Metals & corrosion

Nanomechanical properties of Nb films deposited by pulsed frequency magnetron sputtering

J. G. Medrano[1], J. Raboño-Borbolla[2], O. Cortazar-Martínez[2], A. Herrera-Gómez[2], and F. J. Flores-Ruiz[3],*

[1] *Instituto de Física, Benemérita Universidad Autónoma de Puebla, Ciudad Universitaria, Edif. IF-1, 72570 Puebla, México*

[2] *Centro de Investigación y Estudios Avanzados (CINVESTAV) IPN, Unidad Querétaro, Lib. Norponiente 2000, Real de Juriquilla, 76230 Querétaro, México*

[3] *CONAHCYT–Instituto de Física, Benemérita Universidad Autónoma de Puebla, Edif. IF-1, Ciudad Universitaria, 72570 Puebla, México*

ABSTRACT

The fabrication of niobium-based devices requires precision and reliability and, consequently, the characterization and description of their mechanical properties. However, there are few studies in the literature on mechanical properties characterization, even less so at the nanoscale, where new technologies require this knowledge. In this work, we study the dependence of the morphology, nanomechanical properties, and friction of niobium films on the pulsed frequency during DC sputtering. Niobium films without oxide in their bulk and bcc crystal structure were deposited at room temperature on Si (100) substrate under sputtering pulse frequencies of 20, 100, and 350 kHz. As the pulsed frequency increased, the morphology changed from granular to flake-like, indicating a change in the atomic accommodation due to the increase in the niobium ion energy during the plasma sputtering, which resulted in an increase in the elastic modulus of films. Elastic modulus maps into an area of 1 μm × 1 μm revealed local variations for films with flake-like morphology. Increasing the pulsed frequency in plasma sputtering at 100 and 350 kHz resulted in films with higher elastic modulus flakes and higher attenuation of the ultrasonic wave during nanomechanical mapping, which was related to dissipative forces due to lateral friction, while the granular morphology and lower elastic modulus of films deposited at 20 kHz was associated with friction at interfaces.

Handling Editor: M. Grant Norton.

Address correspondence to E-mail: fflores@ifuap.buap.mx

GRAPHICAL ABSTRACT
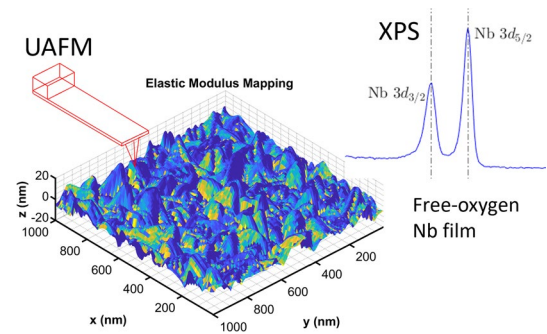
Introduction

Niobium material exhibits mechanical, thermal, chemical, and electrical properties helpful in developing plasmonic devices [1], magnetic shielding layer [2], surface finishing [3], and superconducting radio-frequency cavities [4], among others [5]. For the case of plasmonic applications, it has been found that transition metal nitrides such as TiN [6] and ZrN [7] have similar optical properties to gold with the advantage of being stable at elevated temperatures. Niobium also displays similar optical properties to gold from the near- to the mid-infrared spectral range and has the advantage of having a melting point above 2400 °C [1]. It has been established in Refs. [1, 8, 9] that niobium may be a good candidate for applications in high-temperature plasmonics due to its tunable superfluid plasma frequency [9]. Niobium may absorb and convert light into heat or operate as a selective emission source for thermal radiation unrestricted by low thermal or chemical stability as the noble metals [1]. Besides, Nb is also stable under chemical environments due to its oxide [10].

Along with high chemical stability, superconductor properties [11], and good optical properties, niobium has low density, high Young's modulus, and high yield strength, making it a good candidate in the development of plasmonic devices [5]. Moreover, Nb outperforms TiN and ZrN in ease of preparation [2–4], as it is a single element that does not require a reactive process. Another advantage of niobium over nitrides is its relative ease of fabricating devices using electron beam lithography and plasma etching techniques [1]. On the other hand, in the case of Nb-based superconducting cavities, the photocathode-flange surface requires good mechanical stability

and resistance to scratch formation [12]. Scratches can cause electrical discharges because they can give rise to a high electrical field gradient.

Despite the wide use of niobium in the development of modern devices, only some studies in the literature address the characterization of the mechanical properties of this material deposited by physical vapor deposition or other techniques, without access to mechanical properties mapping. Ramana et al. [5] deposited Nb films (~ 90 nm thick) by radio-frequency sputtering on YSZ (001) substrate maintained at 500 °C and rotating at 3–4 rpm. The resulting films showed (011) and (220) diffractions at $2\theta = 35.9°$ and ~ 81° with cone-like morphology related by the authors with closely packed nanocolumnar epitaxial growth. The mechanical properties of the films were characterized by nanoindentation at indentation depths from 12 to 55 nm. The lower indentation depth (13% of the thickness) gave an elastic modulus of 90 GPa, while an indentation depth of 20 nm gave ~ 240 GPa, where is highly probable that exist a substrate contribution. Seifried et al. [3] deposited Nb coatings (10 μm thick) by DC magnetron sputtering at 250 W (75 mm target diameter) on polished NiTi (50.8% at. Ni) substrate without heating. The resulting films showed (110), (211), and (220) diffractions at $2\theta = $ ~ 38°, 69° and 83°, indicating a polycrystalline structure. The films were characterized by nanoindentation at constant strain rate of 0.05 s^{-1} with indentation depths below of the 10% of the thickness, given an elastic modulus of 98 GPa. Gontad et al. [12] deposited Nb films (~ 60 nm thick) by pulsed laser deposition on Pb substrate. They measured Nb films by nanoindentation obtaining a hardness of 2.8 GPa, but the elastic modulus was not reported.

As seen from previous reports, the mechanical properties are reported as an effective parameter, sufficient in macroscopic applications. However, in developing devices with micro or nanometer sizes, it is necessary to access the local elastic variations within the polycrystalline aggregates. This type of characterization is not available for the case of niobium. In addition, the mechanical properties of Nb films have been characterized on the plastic and elastic–plastic regimens, but the elastic regimen still needs to be studied. To the best of our knowledge, no publications report the mapping of Nb film's mechanical properties at the nanoscale.

This work attempts to fill the knowledge gap in the characterization of nanoscale mechanical properties of niobium films. Here, we study the dependence of the morphology, nanomechanical properties, and friction of niobium films on the pulsed frequency (20, 100, and 350 kHz) during DC sputtering.

Materials and methods

Deposition of Nb films

Nb films were deposited in a high vacuum magnetron sputtering system with a pulsed DC power supply (Advance Energy Pinnacle Plus 3 kW) under three pulsed frequencies to compare, 20, 100, and 350 kHz. A working pressure of 5 mTorr (~0.66 Pa) was used to deposit Nb films from a Nb target (99.95% pure). Prior to each deposition process, the main chamber was evacuated to a base pressure lower than 1×10^{-8} Torr (~ 1.33×10^{-6} Pa). The deposition atmosphere was argon research grade. No intentional heating was applied to the holder substrate during deposition. The holder substrate was maintained at 60 V negative bias voltage to improve the mechanical properties of the resulting films [13] and a 5-rpm rotation to achieve uniformity. Silicon substrates (100) were employed to deposit Nb films, which were ultrasonically cleaned with Alconox, deionized water, acetone, ethanol, and methanol for ten minutes each. Details of the Nb films samples conditions are summarized in Table 1.

Deposition of the aluminum protection layer to prevent niobium oxidation

An aluminum protective layer was deposited on the niobium films to prevent oxidation from environmental exposure. The aluminum protective layer is useful in refractory materials such as niobium since it is employed in photonic structures where good optical stability is required. Protective layers of Al_2O_3 and HfO_2 have been used in metals [14] and refractory materials [15] to improve optical and thermal stabilities. In the present study, the protective layer intends to reveal an oxygen-free niobium deposition during sputtering. Oxygen harms the low-temperature electrical properties of niobium films. It is important to note that the nanomechanical properties, friction, and surface morphology characterizations were performed on the Nb films without protective aluminum layer.

Before depositing the niobium films under the three different pulsed frequency conditions (see Table 1), a niobium film was deposited with the same conditions as the 20 kHz film. Without removing the film from the deposition chamber, a secondary sputtering gun with an aluminum target was activated to deposit a ~ 4.5-nm-thick layer.

XPS measurements on niobium film with protective coating

The niobium film with protective aluminum layer was extracted from the sputtering system and transported to the X-ray photoelectron spectroscopy (XPS) system for characterization. The exposure time to the laboratory environment was approximately 15 min. Measurements were done with an XPS instrument using a monochromatic X-ray aluminum $K\alpha_1$ ($h\nu = 1486.7$ eV) source and a 7-channeltron hemispherical spectrometer. The parameters for the acquisition of the spectra were 10 eV pass energy and 1 eV steps. The angle between

Table 1 Sputtering deposition parameters of Nb films.

Film	Power (W)	Frequency (kHz)	Reversal time (μs)	Rotation (rpm)	Bias voltage (V)	Ar flux (sccm)
Nb_20	150	20	5	5	60	13
Nb_100	150	100	4	5	60	13
Nb_350	150	350	1	5	60	13

the monochromator and the analyzer was 41°, and the measurement angle was 90°.

X-ray diffraction measurements

The structure of the Nb films was investigated by grazing incidence X-ray diffraction (GI XRD). The GI XRD patterns were acquired with a PANalytical X-ray Empyrean diffractometer using Cu Kα radiation ($\lambda = 1.5406$ Å) at grazing incidence of 0.5° and operating at 40 kV and 35 mA. A 2θ scan range from 20° to 80° with 0.05° angle steps was used.

Atomic force microscopy measurements

Morphology characterization

The surface morphology of the niobium films was analyzed with atomic force microscopy (AFM) measurements in an area of 1 μm × 1 μm. AFM measurements were performed in contact mode using an SNL probe within a Bruker Dimension Edge System. From the morphology images, the amplitude distribution function (ADF) was obtained, which gives the probability that a profile has a specific height z at any x position [16]. ADF allows access to statistical parameters such as the root mean square roughness (Rq), skewness, and kurtosis that describe the surface morphology. The Rq measures the average of the measured height deviations taken within the evaluation length and measured from the mean line. The skewness measures the asymmetry of the ADF for a Gaussian distribution; positive skewness indicates that the tail is on the right side of the ADF peak. For the case of AFM images, positive skewness may describe the presence of peaks and/or filled valley on the surface, while negative skewness may point out the presence of grooves without peaks on the surface. The kurtosis parameter is in terms of the tail extremity of the ADF peak; kurtosis indicates outliers that are outside one standard deviation from the mean. In AFM images, the existence of kurtosis may point out the existence of a few high peaks or deep grooves. Bias in statistical parameters due to possible tip-induced wear during contact mode measurements was ruled out by additional tapping mode measurements on a Bruker Innova AFM system.

Nanomechanical characterization

Ultrasonic atomic force microscopy (UAFM) uses a combination of contact with force modulation mode and dynamic AFM modes [17] to access the response amplitude and phase of a tip-sample system as a function of sweep frequency (ω). In this technique, the probe tip is placed in contact with the sample surface, and through a piezoelectric transducer located at the probe's base, longitudinal waves are sent to induce small displacements in the elastic regime at the contact point. The longitudinal wave frequencies are sweep around the contact resonance frequency (ω_0) of the tip-sample system. The contact resonance is one of the eigenmodes of the probe that is sensitive in ω_0 to variations of the normal contact stiffness (k_N) [18]. The amplitude spectrum is fitted to a simple harmonic oscillator model to obtain the relevant parameters as (ω_0) and quality factor (Q value). An initial ansatz for Q value is obtained by dividing ω_0 by the width of the amplitude spectrum at half maximum. The amplitude and phase for mapping are evaluated at ω_0. The ω_0 versus k_N curves can be obtained using analytical equations [19] or finite element analysis (FEA) of the dynamic behavior of the probe [20]. The latter was the approach used in this work and details of the FEA can be found in Refs. [20, 21]. To convert k_N to reduced elastic modulus (E^*), it was determined that between the tip and the specimen there is a plane contact with a radius of the contact area a_C, according to our previous analysis presented in Ref. [18]. Thus, the relationship $k_N = 2 < a_C > E^*$ can be used to calculate the reduced elastic modulus. To access the mapping configuration, nanopositioning control of the AFM tip was used, which ideally avoids tip displacements during the acquisition of amplitude and phase spectra. In the mapping configuration, amplitude and phase spectra are obtained in a grid of M rows by N columns that are usually 128 × 128 to form a three-dimensional data array. Details on the UAFM implementation for mapping can be founded in our previous work [21].

For the case of metals, it is valid to assume that there is almost zero damping at the tip-sample contact, and consequently, the elastic modulus can be obtained from the $k_N (\omega_0)$. The parameter ω_0 provides information about the k_N and can therefore be used to measure the conservative interaction between the tip and the sample. On the other hand, the Q value represents a measure of

dissipative interactions between the tip and the sample, contrasting with the interpretations for viscoelastic materials [22].

Nanofrictional characterization

For the friction measurements, the AFM instrument was operated in contact mode using a probe with diamond-like carbon tip coating. The experimental data were acquired by using the scanning surface profiles while applying a fixed low force to the cantilever [23, 24]. The setpoint parameter in the AFM instrument defines the applied force or load [23, 24]. As the load is given to the film surface (height mode in AFM), surface scanning is done simultaneously (parallel scan to the long axis of the cantilever). This process occurs with a linear increase in the load along the desired swept surface. Then, the friction force is obtained correcting of the topographic profiles forward and backward of the tip travel directions [24]. The applied load and the friction force were calculated following the equations [24]

$$F_N = (S_P + V_D) \times S \times k_{ct}, \tag{1}$$

$$F_F = \frac{\left(\frac{\Delta H}{2}\right) \times k_{ct} \times L}{l_t}. \tag{2}$$

Here S_P is the deflection setpoint (in volts), V_D is the vertical deflection (in volts), S is the sensitivity (in m/volts), k_{ct} is the cantilever spring constant (in N/m), ΔH is the difference in height of the two tip travel directions (forward and backward, in m), L is the length of the cantilever (in m) and l_t is the height of the cantilever tip (in m). Finally, the coefficient of friction is calculated by considering a proportional dependence with the applied load, rewritten in the explicit form

$$\mu = \frac{F_F}{F_N}. \tag{3}$$

Results

XPS, niobium films with and without protective aluminum layer

Figure 1 shows a survey (inspection spectrum) and high-resolution XPS spectra obtained on a niobium
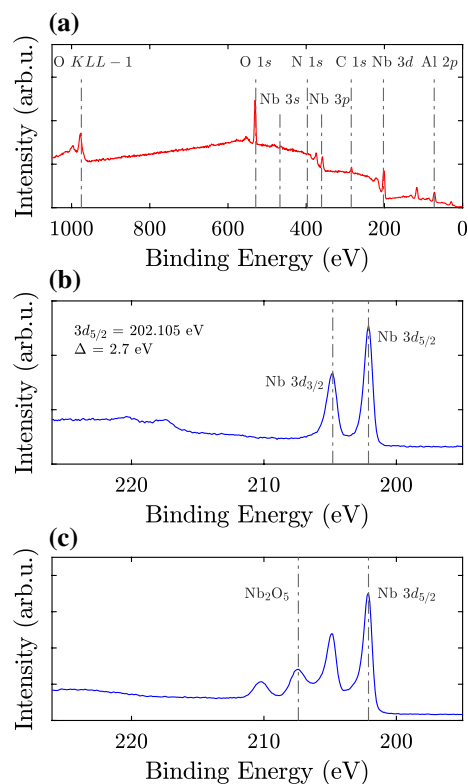
Figure 1 Niobium film (160 nm thick) with a protective aluminum layer of ~ 4.5 nm. (**a**) XPS survey spectrum showing the photoemission of the elements present on the first 8–10 nm of the sample surface. (**b**) High-resolution spectrum for the Nb 3*d* photoemission from the niobium films with protective aluminum layer where there is no oxygen bound to the niobium. (**c**) High-resolution spectrum for the Nb 3*d* photoemission obtained on niobium film (160 nm thick) without a protective aluminum layer.

film with an aluminum protective layer deposited at 20 kHz pulsed frequency. From the low-resolution spectrum [panel (a)], photoemission signal from levels Nb 3*s*, Nb 3*p*, and Nb 3*d* is observed. The photoemission signal Al 2*p* is expected due to the aluminum protective layer. Signals related to oxygen and carbon from the sample surface due to exposition to the environment are also observed.

The high-resolution spectrum for Nb 3*d* photoemission is the most appropriate for investigating the oxide on niobium surfaces [25, 26]. Previous research has shown that in oxygen-free niobium, there is an Nb 3*d* doublet at binding energies between 200 and 206 eV [25, 26]. From Fig. 1b, the Nb 3*d*$_{5/2}$ appears at 202.105 eV and Nb 3*d*$_{3/2}$ at 204.805 eV, with a separation of Δ = 2.7 eV. For comparison, the sample at 20 kHz was also deposited without a protective

aluminum layer, the high-resolution Nb 3d spectrum is presented in panel (c) of Fig. 1. Photoemission indicating the binding of niobium to oxygen is expected to appear from 206 to 212 eV as shown in Refs [25, 26], due to the Nb_2O_5 compound. Figure 1c shows that Nb_2O_5 is present in the niobium film without protective aluminum layer at the expected binding energy, which must be on the surface according to results displayed in Fig. 1b.

XRD results of Nb films

Niobium films were deposited without protective aluminum layer to be analyzed with GI XRD measurements. As mentioned in the materials and methods section, our Nb films were deposited without substrate heating. Figure 2 shows that the GI XRD diffractograms exhibit the (110), (200), and (211) diffraction planes associated with a body-centered cubic (bcc) crystal structure. The dashed vertical lines in the figure indicated the expected positions according to the PDF card No. 01–089-5008 [3]. The diffraction patterns
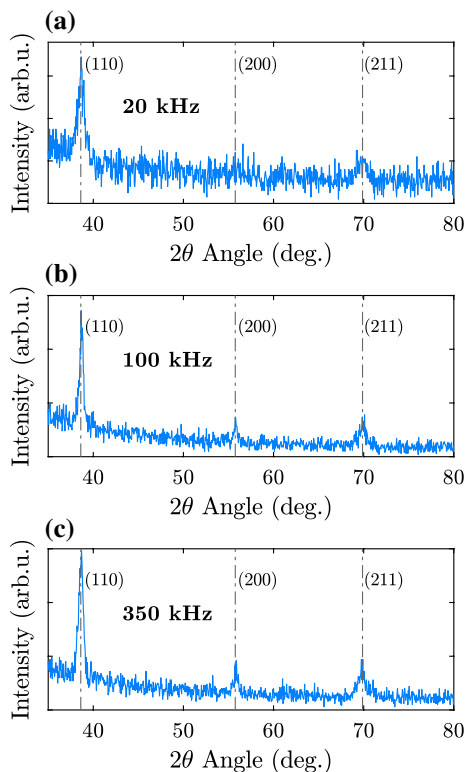
show well XRD intensities, indicating a crystalline growth under the three different pulsed frequency conditions. For the three pulsed frequencies, the (110) diffractions have higher XRD intensities than (200) and (211), indicating that the films tend to grow with (110) orientation, which also has been observed in Nb coatings deposited by DC sputtering [3]. It has been suggested in Ref [3] that the occurrence of reflections (200) and (211) in Nb films may be related to growth and coherence stresses. From the diffractograms in Fig. 2, it is observed that the peak of the diffractions (110) becomes sharper as the pulsed frequency of the DC source increases, which suggests that the Nb films deposited at pulsed frequency of 100 and 350 kHz exhibit grains with a larger size than Nb films deposited at pulsed frequency of 20 kHz.

Surface morphology of the Nb films

Figure 3a–c shows the morphology images of the niobium films deposited under the three pulsed frequency conditions of the DC power supply. The increase in pulsed frequency causes a change in morphology from granular to flake-like, accompanied by a change in the roughness Rq parameter from 3.1 to 7–8 nm. The height distribution functions ADFs for the three pulsed frequency conditions give Gaussian-type profile, as displayed in Fig. 3d. The surface statistical parameters, skewness, and kurtosis were computed from ADF. Table 2 summarizes Rq, skewness, and kurtosis for the niobium films. The table shows that the tails of the ADF shift to the right as the pulsed frequency increases, which gives a positive skewness; this means that a higher pulsed frequency results in surfaces with high peaks and fill valleys. On the other hand, a positive excess kurtosis means that the surface has high peaks and low valleys. The excess kurtosis indicates that there are outliers outside one standard deviation from the mean on the right side of the ADF, as verified in the boxplot in Fig. 3d.

Nanomechanical properties

Figure 4 shows typical raw spectra of amplitude and phase as a function of sweep frequency for a map pixel. The solid blue solid line is the simple harmonic oscillator fit to the amplitude spectrum. The upper right inset in the plots shows values of the maximum amplitude (A_{max}), ω_0, and Q value for each spectrum. Figure 5 shows 1 μm × 1 μm maps of topography,

Figure 2 GI XRD measurements on niobium films deposited at (**a**) 20 kHz, (**b**) 100 kHz, and (**c**) 350 kHz pulsed frequency of DC power supply.

Figure 3 AFM morphology at 1 μm × 1 μm area for niobium films deposited by DC sputtering under pulsed frequency of (**a**) 20 kHz, (**b**) 100 kHz, and (**c**) 350 kHz, (**d**) ADFs and boxplot of the morphology displayed in (**a**–**c**).
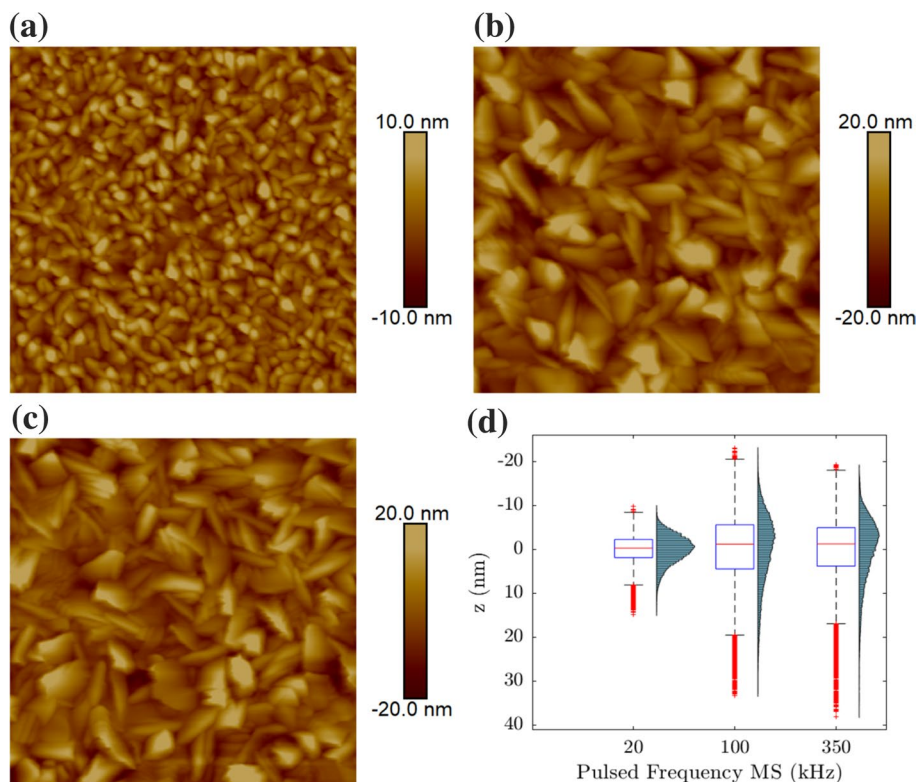

Table 2 Statistical surface parameters of the Nb films.

Sample	Roughness (Rq, nm)	Skewness	Excess Kurtosis
Nb_20 (20 kHz)	3.1	0.45	0.25
Nb_100 (100 kHz)	7.8	0.69	0.49
Nb_350 (350 kHz)	7.2	0.78	1.00

elastic modulus, and Q value obtained simultaneously on niobium films deposited under the three different frequencies pulsed at the DC power source. For the niobium film deposited at 20 kHz, there is a uniform distribution of the elastic modulus and Q value. Increasing the pulsed DC source frequency from 20 to 100 kHz and 350 kHz gives rise to a change in morphology, as described in the previous section, and to a change in the elastic modulus of the sample. Higher pulsed frequency results in regions of tens of nanometer size with higher elastic modulus (see red shades). Three elastic modulus distributions are distinguished in the elastic modulus maps of films deposited at 100 and 350 kHz. The film deposited at 350 kHz shows more significant regions with high elastic modulus. In films deposited at pulsed frequencies of 100 and 350 kHz, regions with red shades in the modulus maps
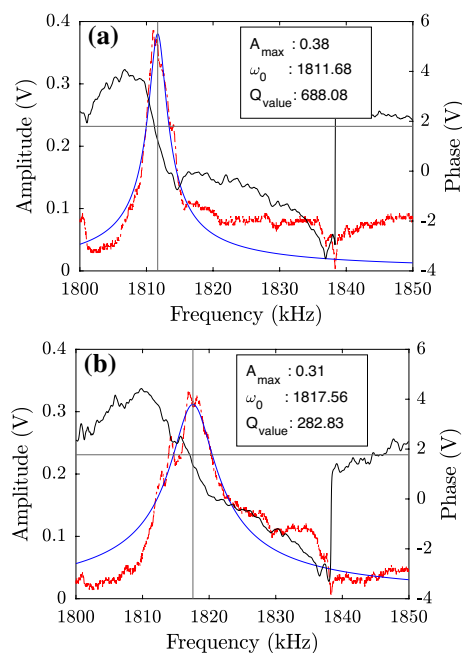
Figure 4 Typical contact resonance UAFM spectra acquired on niobium films deposited at (**a**) 20 kHz and (**b**) 100 kHz. The AFM probe used was a BudgetSensors ContDLC
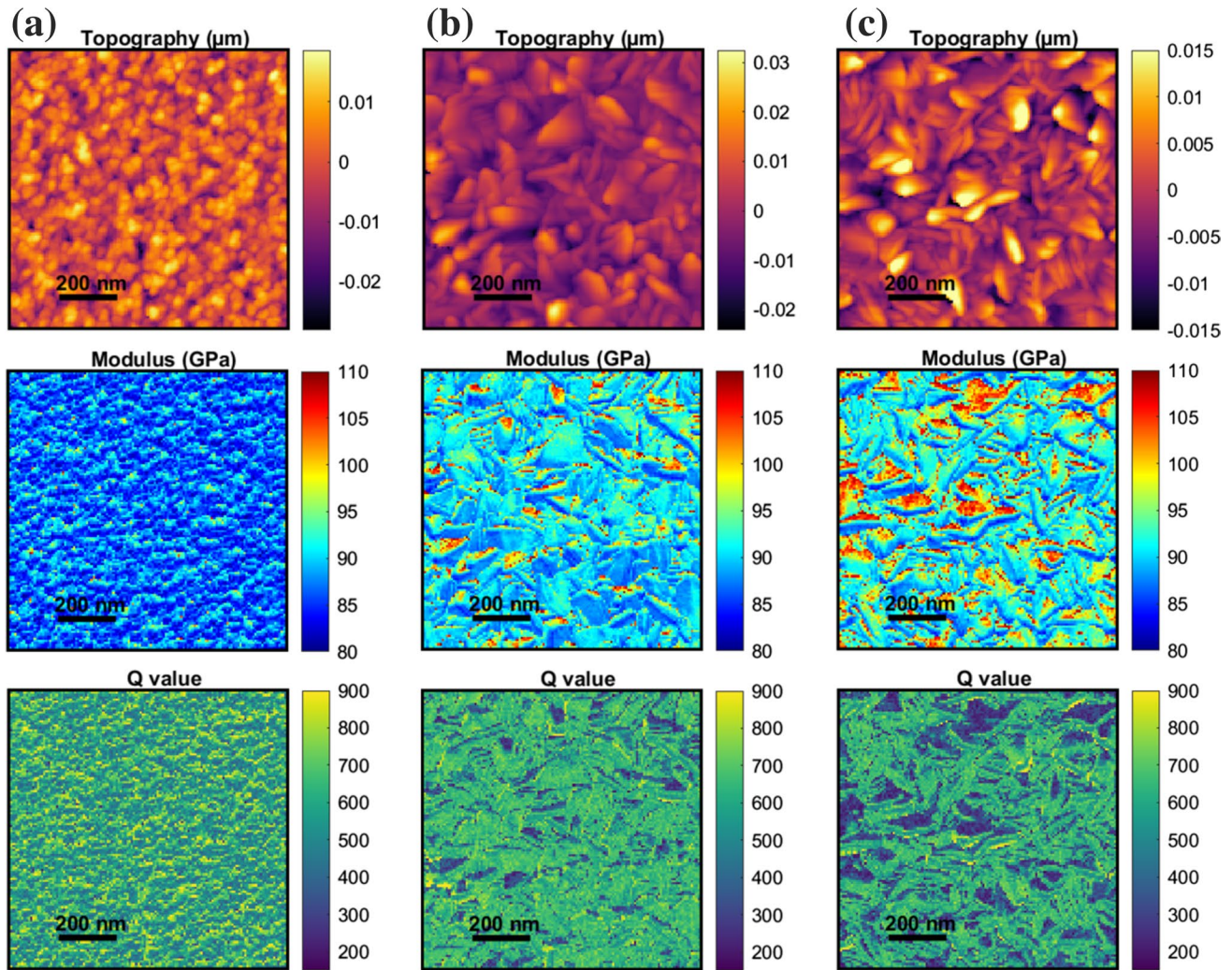
Figure 5 Nanomechanical mapping of niobium films deposited under different pulsed frequencies (**a**) 20 kHz, (**b**) 100 kHz, and (**c**) 350 kHz

present low Q values, indicating that in those regions, the dissipative interactions between the tip and the sample are higher than in regions with low modulus.

The ADFs for the modulus and Q value allow a better appreciation of the changes in the mechanical response of the films as the pulsed frequency of the DC power source increases, see Fig. 6. Increasing the pulsed frequency causes a shift in the ADF of the elastic modulus from symmetric to asymmetric to the right, indicating that regions with higher elastic modulus emerge as the pulsed frequency of the DC power supply increases. Increasing the DC pulsed frequency to 100 kHz results in the appearance of

at least two clear peaks in the Q value, and when increased to 350 kHz, three clear peaks in the Q value are distinguished.

Friction force microscopy

Figure 7 shows friction force (F_F) *vs* load (L) measurements on the niobium films. A linear behavior is observed for all three films, indicating that Amonton's law ($F_F \propto L$) is valid for these measurements at the nanoscale. The values of the nanofriction coefficient are defined by the slope of the fit and are indicated in the graphs. The friction force required to initiate

(a)

(b)
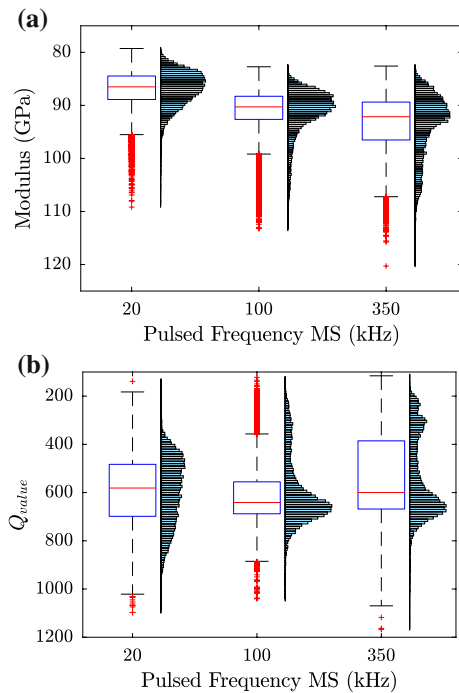
Figure 6 ADFs for (**a**) elastic modulus and (**b**) Q value from the maps displayed in Fig. 5.

sliding at the lowest load is very similar in all three samples, which may be a consequence of the metal surface oxide. However, as the load increases, less friction is required to maintain sliding on the sample deposited at the pulsed frequency of 100 kHz, resulting in a lower coefficient of friction for this sample. The films deposited at pulsed frequency of 100 and 350 kHz have very similar morphology, but the friction force is different. The increase in friction force for the film deposited at 350 kHz seems to be related to the existence of flakes with higher elastic modulus which are seen in the elastic modulus maps (Fig. 5). The flakes with higher elastic modulus also have a lower Q value. Q captures the dissipative forces in UAFM measurements, and in the case of the sample deposited at 350 kHz appear to be related to an increase in frictional force or lateral force.

Discussion

Increasing the pulsed frequency at the DC discharge during the sputtering process caused a change in the morphology and elastic modulus of niobium films. Films deposited with 20 kHz pulsed frequency result in a morphology with a homogeneous distribution of
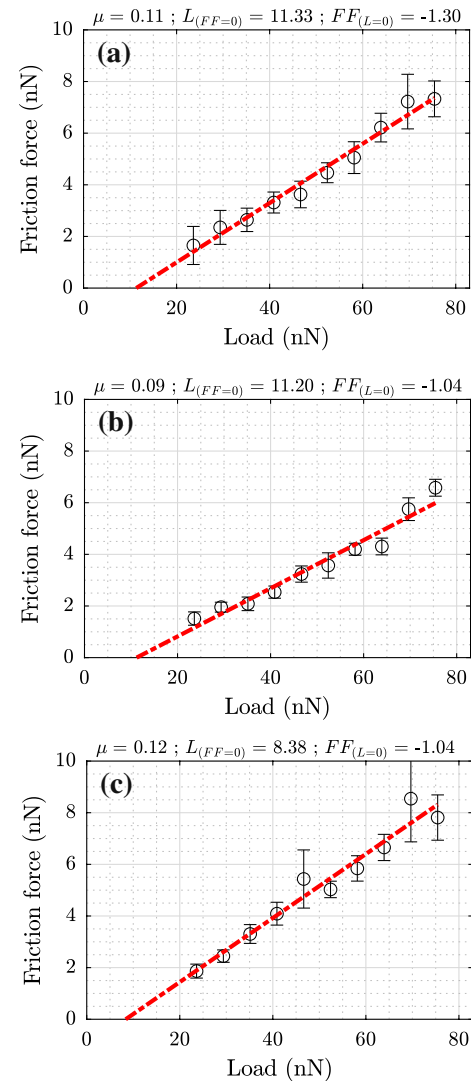
Figure 7 Friction force as a response of the applied load for niobium films deposited at pulsed frequency of (**a**) 20 kHz, (**b**) 100 kHz, and (**c**) 350 kHz. The AFM probe used was a Budget-Sensors ContDLC

grains and an elastic modulus with a symmetric ADF given values of $86.5^{2.39}_{2.04}$ GPa; increasing the pulsed frequency at 100 and 350 kHz result in films with flake-like morphology and asymmetric ADFs for elastic modulus, given values of $90.28^{2.36}_{2.00}$ GPa and $92.13^{4.39}_{2.75}$ GPa, respectively. The films deposited with the pulsed frequency of 100 and 350 kHz show some flakes with elastic modulus ranging from 92.6 to 107.2 GPa. In the elastic modulus maps, each pixel contains information about the integral behavior of the sample in a localized region where the probe tip has induced a higher stress field [27]. The analysis of the mechanical stress

field in a Hertzian contact as a function of penetration depth into the surface indicates that the compressive stress reaches its maximum at the surface and falls off rapidly with the depth into the sample. In contrast, the principal shear stress has its maximum in the sample [28]. Thus, the maximum contrast in elastic modulus comes mainly from the surface of the niobium films and hence from surface features such as granular or flake-like morphology. Table 3 compares our elastic modulus measurements with report from the literature for niobium material. As it can be seen from the table, the average elastic modulus values determined from UAFM maps compare well with other works, with the advantage that UAFM maps provide an elastic modulus distribution.

By comparing the XRD results with the nanomechanical response, there seems to be a relationship of the crystallographic planes present in the films with the local variations of the elastic modulus. The XRD results show that the diffraction peaks become more defined as the pulsed frequency increases. According to a theoretical–experimental study on the bcc metal copper [35], the force required for a displacement of 250 nm with a spherical indenter of radius 3.4 μm is highest for the oriented surface (100), followed by (011) and (111), with forces of 3.82, 3.55, and 3.00 mN, respectively. This behavior can be expected to continue in simple cubic materials with a bcc structure, such as niobium. Following the strain resistance in the bcc copper single crystal for our niobium films,

the (100) orientation should exhibit the highest strain resistance, followed by (110) and (211). These planes are parallel to the substrate, which indicates that the bcc cubic structure has the crystallographic axis [110], [200], and [211] normal to the substrate and parallel to the exerted force by the AFM tip. Since the UAFM technique has the resolution to sense individual grains within polycrystalline aggregates, the increase in the elastic modulus is likely related to the well-defined diffraction peak (110) and (200).

On the other hand, the Q value maps show that the flakes-like aggregates with high elastic modulus have low Q value (see Figs. 4 and 5). As mentioned in the introduction section, the Q value captures the dissipative forces during the ultrasonic vibrations. The dissipative forces in metals or rigid materials usually come from lateral friction, friction at the interface, and internal friction, in contrast to viscoelastic material, where the Q value mainly captures the damping at the tip-sample contact. Although our UAFM measurement method is by nanopositioning control, which contrasts with the tip-probe drag method [21], there are frictional lateral forces at the tip-sample contact that contribute to the attenuation of the detected ultrasonic waves. Friction at interfaces, on the other hand, occurs mainly between the boundaries of different materials within the sample [27]. Our case study deals with single-element material. Even so, the polycrystalline nature of our films results in the existence of polycrystalline aggregates with boundaries where attenuation

Table 3 Comparison between the mechanical properties of Nb from literature and our films.

Reference	Hardness (GPa)	Elastic modulus (GPa)	Morphology	Method used	Deposition method	Test type
[5]	18	240	Cone-like	Nanoindentation	Sputtering	Quasi-static
[3]	–	98, 109	–	Microindentation, Nanoindentation	Sputtering	Quasi-static
[11]	2.8	–	–	Nanoindentation	PLD	Quasi-static
[29]	~4	~80	Grained	Nanoindentation	Sputtering	Quasi-static
[30]	–	63.5	–	AFAM	Sputtering	Single point
[31]	6.6	133	Grained	Nanoindentation	Sputtering	Quasi-static
[32]	4.45–5.39	10–115	Lamelar	Nanoindentation	Sputtering	Single point
[33]	–	77–92	–	Nanoindentation	Sputtering	Quasi-static
[34]	–	113–118	–	AFAM	–	Single point
This work, Nb_20		$86.5_{2.04}^{2.39}$	Grained	UAFM	Sputtering	Mapping
This work, Nb_100		$90.28_{2.00}^{2.36}$	Flake-like	UAFM	Sputtering	Mapping
This work, Nb_350		$92.13_{2.75}^{4.39}$	Flake-like	UAFM	Sputtering	Mapping

of ultrasonic waves may exist. Internal friction occurs within a single material and attenuates the propagation of ultrasonic waves [27]. According to the ADF results for the Q value (Fig. 6b), the sample deposited at a pulsed frequency of 350 kHz presents three distinctive Q values, indicating that there are different friction responses in the flakes. The sample deposited at a pulsed frequency of 100 kHz shows at least two different Q values in its ADF, and thus there are two frictional responses. The frictional lateral forces are likely dominant in the flakes since the flakes have dimensions that exceed the radius of curvature of the tip without abrupt changes of morphology within the flakes. The sample deposited at a pulsed frequency of 20 kHz shows in its ADF a behavior more difficult to decipher since the Q value is ample, indicating that the grains and their boundaries present a distinct frictional behavior. Due to the granular morphology, friction at the interfaces may be responsible for this dissipative behavior.

It has been reported that increasing the frequency in pulsed DC magnetron discharge results in improved ion bombardment of growing films as the physical and chemical characteristics of the plasma becomes time-dependent [23, 24]. Plasma parameters such as energy and incident ion flux influence the structure and properties of the growing films. In particular, for a non-reactive plasma of titanium, it has been observed that the increase in frequency results in an increase in plasma electron temperature, accompanied by a very slight decrease in plasma density, both parameters relative to a DC discharge [24]. Lin et al. [36] observed that increasing pulsed frequency leads to a shift toward higher energies of the ion energy distribution (IED) for the element chromium in a reactive environment. They showed that the IED for the DC discharge shows a peak at an energy of 7 eV for the $^{52}Cr^+$ ion, while the pulsed DC discharge excites a wide range of ion energies up to 65 eV, with peaks of 7–17 eV and 22–32 eV. By comparing DC and pulsed DC discharges for the same reactive condition, they showed that the resulting films have a microstructure ranging from columnar for DC plasmas to a super dense microstructure with a short columnar grain for pulsed DC plasmas. The resulting CrN_x films exhibited hardness values ranging from 22 to 24 GPa for DC plasma to 28–30 GPa for pulsed DC plasma in a 20–70% nitrogen flow rate environment. In addition, pulsed plasma resulted in CrN_x films that exhibit a lower coefficient of friction and wear rate than DC plasma films.

Considering the beneficial evidence of pulsed plasma, it is possible to understand the increase in the elastic modulus of our niobium films and the change in morphology, the increase in the pulsed frequency results in a plasma with high ionization density and higher electron temperature. As the frequency is increased, ions with higher kinetic energy reach the substrate and transfer their energy to the adsorbed atoms lying on the surface of the growing film. The energy transfer increases the mobility of these surface atoms, which seal vacancies and create more nucleation sites [36]. This process increases the density of the growing film and consequently improves its mechanical properties.

In summary, according to X-ray photoelectron spectroscopy, it was observed that the bulk of our films is oxygen-free, which required the deposition of a ~ 4.5-nm-thick aluminum protective layer to avoid surface oxidation. Nanomechanical characterization was performed on films without a protective aluminum layer with ultrasonic atomic force microscopy (UAFM) assisted with resonance tracking (RT). Nanofriction of the films was accessed with friction force microscopy technique. Our results shown that increasing the pulsed frequency results in a change of morphology from granular to flake-like. An increase in the elastic modulus accompanies the change of morphology. Films with flake-like morphology exhibit local elastic variations that allow distinguishing at least two different values of elastic modulus. Films with flake-like morphology have flakes with a high elastic modulus but exhibit a higher attenuation of the ultrasonic wave during nanomechanical mapping. In these flakes, the dissipative interaction between the tip and sample surface is dominated by lateral friction. In contrast, in films with granular morphology, the dissipative interaction is by friction at the interfaces.

Conclusions

In this study, we have reported the nanomechanical properties of niobium films deposited by magnetron sputtering using a DC power supply operating under three pulsed frequency conditions, 20, 100, 350 kHz. First, we deposited niobium films with and without a protective layer of aluminum to show that the bulk of our films is oxygen-free. The bulk of the film gave photoelectron XPS signals related to Nb $3d_{5/2}$ and Nb $3d_{3/2}$ without contributions associated with

the Nb_2O_5 compound. XRD diffractograms reveal a body-centered-cubic crystal structure of the films with a tend to grow with (110) orientation. Nanomechanical mapping of the niobium films without an aluminum protective layer was obtained under the three pulsed plasma conditions. It was found that as the pulsed frequency increases, the morphology changes from granular to flake-like and the elastic modulus increases. Maps of the resonant peak quality factor obtained during nanomechanical mapping indicate that there are flakes in the films deposited at 100 and 350 kHz that cause a higher attenuation of the ultrasonic wave, i.e., they present a lower Q value. Films deposited at the pulsed frequency of 350 kHz have a higher number of flakes with a lower *Q* value. Such films also presented a higher coefficient of friction than the film deposited at 100 kHz. Thus, the Q value of the nanomechanical mapping was related to the friction coefficient of the samples. The responsible for the improvement in the elastic modulus and appearance of the flake-like morphology is the increase in the energy of the niobium ions that reach the substrate in the pulsed plasma. These ions transfer their energy to the adsorbed atoms on the surface of the growing film, thereby increasing the mobility of the surface atoms, which in turn fills vacancies and creates nucleation sites, resulting in a denser film with enhanced mechanical properties. This enhancement in the densification also results in better-defined diffraction peaks.

Acknowledgements

Author's contribution

JGM was involved in writing—original draft, visualization, conceptualization, investigation. JRB, OCM, and AEG helped in validation, investigation, data curation. FJFR contributed to funding acquisition, visualization, investigation, supervision.

Data availability

The raw data can be accessed on request from the corresponding author.

Declarations

Competing interest The authors declare that they have no known competing financial interests or personal relationships that could have appeared to influence the work reported in this paper. On behalf of all authors, the corresponding author states that there is no conflict of interest.

Ethical approval This manuscript does not contain any human or animal experiments.

References

[1] Bagheri S, Strohfeldt N, Ubl M, Berrier A, Merker M, Richter G, Siegel M, Giessen H (2018) Niobium as alternative material for refractory and active plasmonics. ACS Photonics 5:3298–3304. https://doi.org/10.1021/acsphotonics.8b00530

[2] Wilde S, Valizadeh R, Malyshev OB, Stenning GBG, Sian T, Chesca B (2018) dc magnetometry of niobium thin film superconductors deposited using high power impulse magnetron sputtering. Phys Rev Accel Beams 073101:1–12. https://doi.org/10.1103/PhysRevAccelBeams.21.073101

[3] Seifried F, Leiste H, Schwaiger R, Ulrich S, Seifert HJ, Stueber M (2018) Structure, morphology and selected mechanical properties of magnetron sputtered (Mo, Ta, Nb) thin films on NiTi shape memory alloys. Surf Coat Technol 347:379–389. https://doi.org/10.1016/j.surfcoat.2018.05.014

[4] Li M, Pu G, Luo Y, Ye Z, Wei J, Chen S, Wu A, Yang L (2021) The investigation of chemical vapor deposited copper-based niobium films. Mater Res Express 8:046402–046415

[5] Ramana CV, Makeswaran N, Zade V, Das D, Tan S, Xu S, Beyerlein IJ (2022) Fabrication and characterization of high-quality epitaxial nanocolumnar Niobium films with abrupt interfaces on YSZ(001). Phys Chem C. https://doi.org/10.1021/acs.jpcc.1c08738

[6] Bagheri S, Zgrabik CM, Gissibl T, Tittl A, Sterl F, Walter R, De Zuani S, Berrier A, Stauden T, Hu EL, Giessen H (2015) Large-area fabrication of TiN nanoantenna arrays for refractory plasmonics in the mid- infrared by

femtosecond direct laser writing and interference lithography [Invited]. Opt Mater Express 5:7998–8006. https://doi.org/10.1364/OME.5.002625

[7] Guler U, Technologies R, Naik G, Kildishev AV (2012) Performance analysis of nitride alternative plasmonic materials for localized surface plasmon applications Performance analysis of nitride alternative plasmonic materials for localized surface plasmon applications. Appl Phys B Lasers Opt 107:5708–5713. https://doi.org/10.1007/s00340-012-4955-3

[8] West PR, Ishii S, Naik GV, Emani NK, Shalaev VM (2010) Searching for better plasmonic materials. Laser Photon Rev 808:795–808. https://doi.org/10.1002/lpor.200900055

[9] Kurter C, Abrahams J, Shvets G, Anlage SM (2013) Plasmonic scaling of superconducting metamaterials. Phys Rev 180510:1–5. https://doi.org/10.1103/PhysRevB.88.180510

[10] Skliarova H, Azzolini O, Cherenkova-Dousset O, Johnson RR, Palmieri V (2014) Niobium-based sputtered thin films for corrosion protection of proton-irradiated liquid water targets for [18F] production. J Phys D Appl Phys 47:45306–45317. https://doi.org/10.1088/0022-3727/47/4/045306

[11] Berti G, Torres-Castanedo CG, Goronzy DP, Bedzyk MJ, Hersam MC, Kopas C, Marshall J, Iavarone M (2023) Scanning tunneling microscopy and spectroscopy characterization of Nb films for quantum applications. Appl Phys Lett 122:192605–192611. https://doi.org/10.1063/5.0145090

[12] Gontad F, Lorusso A, Panareo M, Monteduro AG, Maruccio G (2015) Nanomechanical and electrical properties of Nb thin films deposited on Pb substrates by pulsed laser deposition as a new concept photocathode for superconductor cavities. Nucl Instrum Methods Phys Res A 804:132–136. https://doi.org/10.1016/j.nima.2015.09.064

[13] Audronis M, Leyland A, Kelly PJ, Matthews A (2006) The effect of pulsed magnetron sputtering on the structure and mechanical properties of CrB2 coatings. Surf Coat Technol 201:3970–3976. https://doi.org/10.1016/j.surfcoat.2006.08.006

[14] Albrecht G, Ubl M, Kaiser S, Giessen H, Hentschel M (2018) Comprehensive study of plasmonic materials in the visible and near- infrared: linear, refractory, and nonlinear optical properties. ACS Photonics 5:1058–1067. https://doi.org/10.1021/acsphotonics.7b01346

[15] Park JH, Han SE, Nagpal P, Norris DJ (2016) Observation of thermal beaming from tungsten and molybdenum Bull's eyes. ACS Photonics 3:494–500. https://doi.org/10.1021/acsphotonics.6b00022

[16] Nečas D, Klapetek P (2012) Gwyddion: an open-source software for SPM data analysis. Cent Eur J Phys 10:181–188. https://doi.org/10.2478/s11534-011-0096-2

[17] Stan G, Solares SD (2014) Frequency, amplitude, and phase measurements in contact resonance atomic force microscopies. Beilstein J Nanotechnol 5:278–288. https://doi.org/10.3762/bjnano.5.30

[18] Flores-Ruiz FJ, Espinoza-Beltrán FJ, Diliegros-Godines CJ, Siqueiros JM, Herrera-Gómez A (2016) Atomic force acoustic microscopy: influence of the lateral contact stiffness on the elastic measurements. Ultrasonics 71:271–277. https://doi.org/10.1016/j.ultras.2016.07.003

[19] Rabe U (2006) Atomic force acoustic microscopy. In: Bhushan B, Fuchs H (Eds), Appl. Scanning Probe Methods II Scanning Probe Microsc. Tech., Springer Berlin Heidelberg, Berlin, Heidelberg, pp 37–90. https://doi.org/10.1007/3-540-27453-7_2

[20] Espinoza-Beltrán FJ, Geng K, Muñoz Saldaña J, Rabe U, Hirsekorn S, Arnold W (2009) Simulation of vibrational resonances of stiff AFM cantilevers by finite element methods. New J Phys 11:083034–083056. https://doi.org/10.1088/1367-2630/11/8/083034

[21] Garduño-Medina A, Muñoz-Pineda E, Vázquez-Delgado MA, Garcia-Vazquez V, Espinosa-Luna R, Flores-Ruiz FJ (2021) AFM measurement of the cuticle of the orchid bee Euglossa sp.: elastic properties under dehydrated and hydrated conditions. Measurement 185:110045–110060. https://doi.org/10.1016/j.measurement.2021.110045

[22] Taleb S, Badillo M, Flores-Ruiz FJ, Acuautla M (2023) From synthesis to application: high-quality flexible piezoelectric sensors fabricated from tetragonal BaTiO3/ P(VDF-TrFE) composites. Sens Actuators A Phys 361:114585–114596. https://doi.org/10.1016/j.sna.2023.114585

[23] Vlcek J, Pajdarov AD, Musil J (2004) Pulsed dc magnetron discharges and their utilization in plasma surface engineering. Plasma Phys 44:426–436. https://doi.org/10.1002/ctpp.2004100

[24] Bradley JW, Backer H, Aranda-Gonzalvo Y, Kelly PJ, Arnell RD (2002) The distribution of ion energies at the substrate in an asymmetric bi-polar pulsed DC magnetron discharge. Plasma Sour Sci Technol 11:165–174

[25] Ma Q, Rosenberg RA (2003) Angle-resolved X-ray photoelectron spectroscopy study of the oxides on Nb surfaces for superconducting r. f. cavity applications. Appl Surf Sci 206:209–217

[26] Ma Q, Ryan P, Freeland JW, Rosenberg RA (2004) Thermal effect on the oxides on Nb (100) studied by synchrotron-radiation X- ray photoelectron spectroscopy. J Appl Phys 96:7675–7680. https://doi.org/10.1063/1.1809774

[27] Sharahi HJ, Janmaleki M, Tetard L, Kim S, Sadeghian H, Verbiest GJ (2021) Acoustic subsurface-atomic force microscopy: three- dimensional imaging at the nanoscale. J Appl Phys 129:030901–030922. https://doi.org/10.1063/5.0035151

[28] Rabe U, Kopycinska-Müller M, Hirsekorn S (2013) Atomic force acoustic microscopy. In: Acoust Scanning Probe Microsc, pp 315–350. https://doi.org/10.1007/978-3-642-27494-7

[29] Khamseh S, Alibakhshi E, Ramezanzadeh B, Sari MG, Nezhad AK (2020) Developing a graphite like carbon: niobium thin film on GTD-450 stainless steel substrate. Appl Surf Sci 511:145613–145623. https://doi.org/10.1016/j.apsusc.2020.145613

[30] Hurley DC, Shen K, Jennett NM, Turner JA (2003) Atomic force acoustic microscopy methods to determine thin-film elastic properties. J Appl Phys 94:2347–2354. https://doi.org/10.1063/1.1592632

[31] Xu Z, Yate L, Qiu Y, Aperador W, Coy E, Jiang B, Moya S, Wang G, Pan H (2019) Potential of niobium-based thin films as a protective and osteogenic coating for dental implants: the role of the nonmetal elements. Mater Sci Eng C 96:166–175. https://doi.org/10.1016/j.msec.2018.10.091

[32] Li X, Cao WH, Tao XF, Ren LL, Zhou LQ, Xu GF (2016) Structural and nanomechanical characterization of niobium films deposited by DC magnetron sputtering. Appl Phys A 122:505–511. https://doi.org/10.1007/s00339-016-9990-1

[33] Zgheib E, Alhussein A, Slim MF, Khalil K, François M (2019) Multilayered models for determining the Young's modulus of thin films by means of Impulse Excitation Technique. Mech Mater 137:103143–103160. https://doi.org/10.1016/j.mechmat.2019.103143

[34] Kopycinska-Müller M, Striegler A, Köhler B, Wolter K-J (2011) Mechanical characterization of thin films by use of atomic force acoustic microscopy. Adv Eng Mater 13:312–318. https://doi.org/10.1002/adem.201000245

[35] Liu Y, Varghese S, Ma J, Yoshino M, Lu H, Komanduri R (2015) Orientation effects in nanoindentation of single crystal copper. Int J Plast 24:1990–2015. https://doi.org/10.1016/j.ijplas.2008.02.009

[36] Lin J, Wu ZL, Zhang XH, Mishra B, Moore JJ, Sproul WD (2009) A comparative study of CrNx coatings synthesized by dc and pulsed dc magnetron sputtering. Thin Solid Films 517:1887–1894. https://doi.org/10.1016/j.tsf.2008.09.093